IEEE Access
Multidisciplinary | Rapid Review | Open Access Journal

Received May 4, 2021, accepted May 18, 2021, date of publication May 24, 2021, date of current version June 2, 2021.

Digital Object Identifier 10.1109/ACCESS.2021.3082996

Design of V-Type Consequent-Pole IPM Machine for PM Cost Reduction With Analytical Method

JUNG-WOO KWON, MINGJIE LI, AND BYUNG-IL KWON, (Senior Member, IEEE)
Department of Electronic Engineering, Hanyang University, Ansan 15588, South Korea

Corresponding author: Byung-Il Kwon (bikwon@hanyang.ac.kr)

This work was supported in part by the National Research Foundation of Korea (NRF) grant funded by the Korea Government (MSIT) under Grant NRF-2020R1A2B5B01002400, and in part by the BK21FOUR Program through the National Research Foundation of Korea within the Ministry of Education.

ABSTRACT This study proposes an analytical method (AM) for V-type consequent-pole permanent magnet (V-CPM) machines to quickly determine the suitable permanent magnet (PM) volume while reducing the PM volume compared to that of the V-type interior PM (V-IPM) machine. Special air-gap magnetic flux density modeling is adopted in the AM, which consists of 4 asymmetric regions under one PM and the iron pole of the V-CPM. This specific modeling is utilized for the V-CPM topology, which has a different magnetic saturation trend from the conventional surface-mounted CPM (S-CPM). Hence, additional consideration of rotor saturation by novel method has been done compared to the previous works. To achieve average torque similar to that of the V-IPM machine, a V-CPM machine is designed by the proposed AM to have the same fundamental harmonic value of air-gap flux density. Furthermore, two conditions are considered for the V-CPM machine design to prevent unnecessary saturation and to minimize torque ripple. All the performance metrics of the designed V-CPM machine are compared with those of the other machines to demonstrate its superiority.

INDEX TERMS V-type consequent-pole, interior permanent magnet (IPM) machine, analytical method, air-gap flux density.

I. INTRODUCTION

The V-type interior permanent magnet (V-IPM) machine is widely used in industrial and home applications, owing to its high torque density and high efficiency [1]. Compared with the surface permanent magnet (SPM) machine, the V-IPM machine offers a higher torque density, wider flux-weakening speed range, no need of sleeve, and higher efficiency [2], [3]. However, with the increase in the price of permanent magnet (PM) materials, the manufacturing cost of PM machines has increased. Therefore, reducing the PM volume in PM machines has become important.

To decrease the PM volume, the consequent-pole permanent magnet (CPM) has attracted much attention [4]–[8]. Depending on the application, the research targets for employing the CPM structure vary and can be divided into 2 types. First, some studies focus on improving the output performance, which is based on a similar PM volume to that of the investigated machine [5]. Second, for a similar output performance to that of the investigated machine, the PM volume reduction is the key target [4], [6], [8]. In [4], the quasi-trapezoidal PM is employed in the CPM machine to improve the torque and reduce the volume of the PM; meanwhile, the total harmonics of back-EMF is reduced and the proposed structure shows stronger demagnetization capability. In [5] and [6], the CPM machine with the staggered rotor is investigated while the even-order harmonics of the phase back-EMFs are eliminated. The axial magnetized PM is embedded in the middle of the rotor in this CPM structure to improve the air-gap flux density and output torque. From [4] to [6], the CPM is widely used based on the SPM structure. In contrast, a spoke-type CPM machine with the asymmetric rotor is proposed [7]. The spoke-type CPM has proven to have a large output torque and low torque ripple. In [8], the pole-shaping method combined with the V-type CPM (V-CPM) structure is employed to provide the flux-focusing effect, whereas the V-CPM structure can increase the PM utilization and decrease the PM volume.

The associate editor coordinating the review of this manuscript and approving it for publication was Yi Ren.

Most existing studies of CPM were based on the finite-element method (FEM) which is time-consuming [9], [10]. In contrast to FEM, the AM is fast and can clearly reflect the relationship between the magnetic field and machine parameters [11], [12]. However, few studies focused on the analytical method (AM), most of which were based on surface-mounted CPM (S-CPM) machines. In [13], AM is adopted to find the optimum pole number for the bearing-less S-CPM machine to produce small oscillations of the magnetic suspension force. The magnetic suspension force is calculated based on the air-gap flux-density distribution. In [14], the AM based on the approximation calculation of the magnetic flux distribution in the air gap is proposed to investigate the voltage harmonic characteristics. The results show that a specific number of slots in the concentrated winding could eliminate the even-order harmonics of the induced EMF. In [15] and [16], the partial differential equations derived from Maxwell's equations are used as the AM to investigate the magnetic flux density of the S-CPM with an inner and outer rotor, respectively. In [17], an AM based on the magnetic equivalent circuit of the S-CPM machine is proposed to derive the optimal pole-arc ratio, the result shows that the optimal pole-arc ratio is determined by the ratio of the air-gap length to the PM thickness. In [18], the optimal split ratio and the optimal pole-arc ratio of the S-CPM machine are considered simultaneously; the analytical method is the same as that in [17]. However, the previous AMs of the S-CPM machines cannot be employed directly in the IPM machines with CPM structure. This is due to the different magnetic saturation of the rotor part in the V-CPM machines compared to the S-CPM machines. In the S-CPM machine, the rotor saturation is usually neglected, owing to its negligible area [17]. However, the rotor saturation in the V-CPM machine is focused on the rib bridge, which is rather thick for its suitable mechanical strength [8], [20]. This indicates that the magnetic saturation of the rib bridge must be considered additionally in the V-CPM machine analysis. The method of utilizing AM for designing has been done multiple times for S-CPM machines as can be seen from numerous references [11]–[19]. However, method of utilizing AM for designing V-CPM machines considering its unique topology hasn't been done properly.

In this paper, an AM is proposed for the V-CPM machine to determine the suitable PM volume quickly. Because of the unique topology of V-CPM, additional magnetic saturation on the rotor part was considered in the proposed AM. In Section II, the topologies of the V-IPM machine and the investigated V-CPM machine are described. In Section III, the AM is proposed to analyze the air-gap flux-density distribution of the V-IPM machine and V-CPM machine. In Section IV, a V-CPM machine with less PM volume is designed. Parameters are derived under the proposed AM, to achieve a similar average torque with the V-IPM machine. The open-circuit air-gap flux density, Back-EMF, the torque performance of the designed V-CPM is evaluated and compared with the V-IPM machine with FEM. Finally, Section V states the conclusion.

II. TOPOLOGIES

For the V-IPM machine, a stator slot and rotor pole combination of 40 slots and 8 poles with five phases have been a great example, especially for reducing the torque ripple [21]. This is considered in the early stage of design as the consequent pole structure causes high cogging torque hence high torque ripple. Figure 1 (a) and (b) describes the stator and rotor of the conventional V-IPM machine, respectively. Winding layout can be seen in Figure 1 (a), which is five phase integral slot distributed winding with single layer. This is adopted as a reference. The parameters of the conventional V-IPM machine are listed in Table 1.

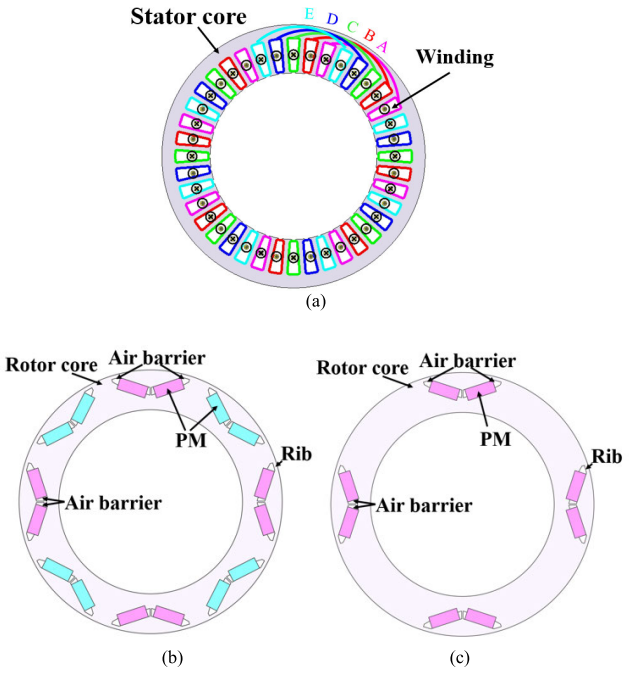

FIGURE 1. 40-slots/8-poles PM machine with different rotor structures (a) 40-slots stator with winding layout. (b) Conventional V-IPM rotor. (c) V-CPM rotor.

To decrease the PM volume, the consequent-pole PM structure has been applied in the conventional V-IPM rotor as shown in Figure 1 (c), [8]. As can be seen from the figure, one of the two PM poles is substituted with an iron core. The basic parameters shown in Table 1 are held the same for all the investigated machines, such as the stator parameters, stack length, air-gap length, phase current, and materials.

This paper aims to design a V-CPM machine that achieves similar average torque to that of the V-IPM machine while having decreased PM volume. To design the V-CPM machine, the rotor parameters are selected with the aid of the proposed AM.

TABLE 1. Specification of the conventional V-IPM machine.

Item	Unit	Conventional V-IPM machine
Stator slot/rotor pole	-	40/8
Number of phases	-	5
Stator outer diameter	mm	155
Air-gap length	mm	0.5
Rotor outer diameter	mm	97
Effective length	mm	46
PM length	mm	10.8
PM width	mm	4.3
Rated speed	rpm	1500
Rated current	A	10.8
Turns per phase		40
PM remanence	T	1.2
Steel saturated remanence	T	1.8

III. ANALYTICAL METHOD FOR AIR-GAP FLUX DENSITY

A. V-IPM MACHINE

The following assumptions were made for the proposed AM:

1. The saturation of the stator steel is ignored.
2. The slotting effects of all investigated machines are ignored.

The graphical representation of the saturation and air-gap regions under one pole pair in the V-IPM machine is shown in Figure 2. The magnetic saturation of the rotor iron occurs in the rib which is highlighted as yellow as shown in Figure 2 [21]. The general details of the flux distribution based on the analytical method are referred from [11] and [22]. From these references, the complicated flux paths in the rotor of the V-IPM machine are shown. To simplify the flux path, the proposed AM only includes half of a single pole-pair and its corresponded flux line, as the flux paths of a single pole-pair are symmetric.

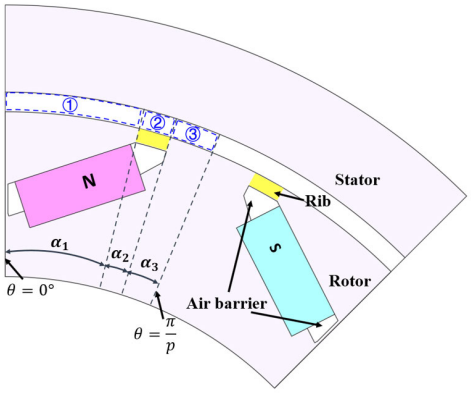

FIGURE 2. 1/8 of the V-IPM machine with the graphical description and air-gap regions.

The air gap facing the PM, air barrier, and iron of the half pole is divided into three regions, which can be seen in Figure 2 as Region ①, ②, and ③, respectively. In Figure 2, α_1, α_2, and α_3 are the angles of Regions ①, ②, and ③, respectively. α_2 is the angle of the air barrier. The slotless air-gap flux density waveform with the trapezoidal waveform in the V-IPM machine is shown in Figure 3 [23]. In Region ①, the flux lines pass uniformly through the air gap into the stator, which results in the constant slotless air-gap flux density B_{m_m}. B_{m_m} is the maximum value of the slotless air-gap flux density. As the magnetic flux tends to flow through the lowest reluctance path the slotless air-gap flux density in Region ③ can be assumed to be zero. Region ② is sandwiched between Region ① and Region ③, and the slotless air-gap flux density is assumed to decrease from its maximum value to zero. The slotless air-gap flux-density distribution of the S-Pole is symmetric to that of the N-pole. [21]

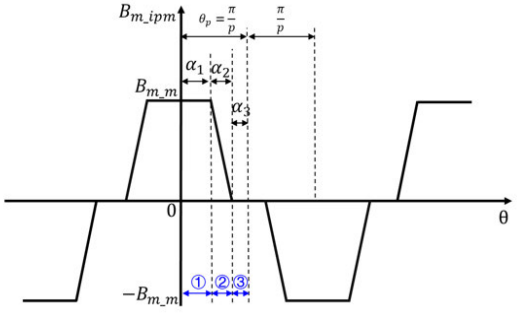

FIGURE 3. Waveform modeling of the slotless air-gap flux density of the V-IPM machine.

The magnetic flux paths of the V-IPM machine are shown in Figure 4. In general, the reluctance of stator steel R_s and the reluctance of rotor steel R_r are neglected. This is because the permeability of steel is much higher than that of the air gap or PMs when there is no significant magnetic saturation in steel. By placing the air barriers beside the PMs, the end flux leakage of PMs will be reduced. Due to the air barriers, rotor iron bridge will be saturated and then act as air gap rather than flux leakage path. Because the flux path which crosses air barriers has a very small portion of magnetic flux density

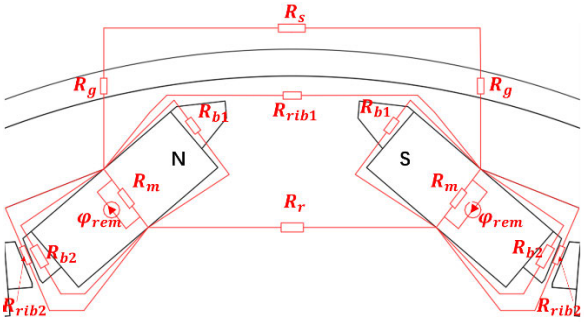

FIGURE 4. Flux paths of the V-IPM machine.

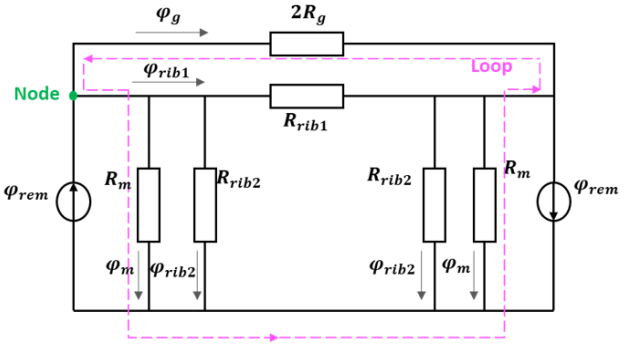

FIGURE 5. Magnetic equivalent circuit of the V-IPM machine.

compared to other flux paths, the reluctances of air barriers R_{b1} and R_{b2} are neglected, [24], [12]. The simplified magnetic equivalent circuit is shown in Figure 5.

In Figure 5, φ_{rem} is the flux source of the PM. φ_m and φ_g are the PM flux and air-gap flux, respectively. R_g and R_m are the reluctance of the air gap and PM, and φ_{rib2} are the flux passing through the two different ribs. Unlike that of the SPM machine, the rotor saturation of the V-IPM machine is considered in the magnetic equivalent circuit. R_{rib1} and R_{rib2} are the corresponding reluctances of two different saturation ribs. By applying Kirchhoff's law, the magnetic equivalent circuit equations are expressed as

$$\text{Node:}\varphi_{rem} = \varphi_g + \varphi_{rib1} + \varphi_{rib2} + \varphi_m, \tag{1}$$

$$\text{Loop:}2^*\varphi_g^* R_g = 2^*\varphi_m^* R_m. \tag{2}$$

Then, the air-gap flux φ_g can be calculated as

$$\varphi_g = (\varphi_{rem} - \varphi_{rib1} - \varphi_{rib2})^*(\frac{R_m}{R_m + R_g}) \tag{3}$$

and the parameters in Eq. (3) can be expressed as

$$\varphi_{rem} = B_r^* h_{pm}^* l_{stk}, \tag{4}$$

$$\varphi_{rib1} = B_{sat}^* l_{rib1}^* l_{stk}, \tag{5}$$

$$\varphi_{rib1} = B_{sat}^* \frac{l_{rib2}}{2}^* l_{stk}, \tag{6}$$

where B_r is the residual flux of the PM, h_{pm} is the thickness of PM, l_{pm} is the length of the PM, and l_{rib1} and l_{rib2} are the thicknesses of iron ribs 1 and 2, respectively. These parameters and others to be discussed are shown in Figure 6 for a better description.

B_{sat} is the saturation flux density of iron steel, μ_0 is the permeability of a vacuum, μ_r is the relative permeability of PM, and l_{stk} is the stack length of the machine.

The air-gap reluctance is related to the pole arc angle. α_4 is half of the pole arc angle of the N-pole, which is the sum of α_1 and α_2. The PM and air-gap reluctances can be expressed as

$$\begin{cases} R_m = \dfrac{h_{pm}}{\mu_o \mu_r l_{pm} l_{stk}} \\ R_g = \dfrac{g}{\mu_o (R + \frac{g}{2})\alpha_4 l_{stk}} = \dfrac{g}{\mu_o (R + \frac{g}{2})(\alpha_1 + \alpha_2) l_{stk}} \end{cases} \tag{7}$$

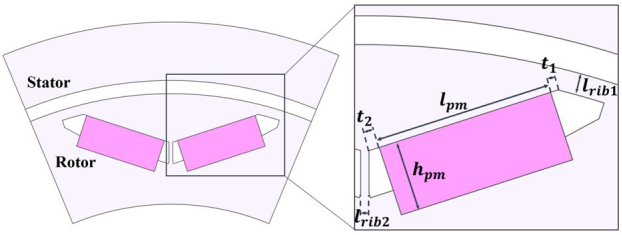

FIGURE 6. Parameters of the V-type PM for the equations.

where R and g are the rotor outer radius and thickness of the air-gap length, respectively.

Meanwhile, the relationship between the air-gap flux density B_{m_ipm} and the air-gap flux φ_g can be expressed as

$$\varphi_g = \int_0^{\theta_p} B_{m\_ipm}(\theta)(R + \frac{g}{2}) l_{stk} d\theta, \tag{8}$$

where θ_p is half the pole-pitch angle of one PM. In a V-IPM machine, the value of θ_p is equal to π/p.

By substituting Eq. (1)–(7) into (8), the maximum value of the slotless air-gap flux density can be expressed as

$$B_{m\_m} = \frac{\varphi_g}{(R + \frac{g}{2})(\alpha_1 + \frac{\alpha_2}{2}) l_{stk}}. \tag{9}$$

The slotless air-gap flux density B_{m_ipm} could also be expressed as

$$B_{m\_m} = \begin{cases} B_{m\_m} & (0 \le \theta < \alpha_1) \\ \dfrac{B_{m\_m}}{\alpha_2}(\alpha_1 + \alpha_2 - \theta) & (\alpha_1 \le \theta < \alpha_1 + \alpha_2) \\ 0 & (\alpha_1 + \alpha_2 \le \theta < \dfrac{2\pi}{p} - \alpha_1 - \alpha_2) \\ \dfrac{-B_{m\_m}}{\alpha_2}(\theta - \dfrac{2\pi}{p} + \alpha_1 + \alpha_2) & \\ & (\dfrac{2\pi}{p} - \alpha_1 - \alpha_2 \le \theta < \dfrac{2\pi}{p} - \alpha_1) \\ -B_{m\_m} & (\dfrac{2\pi}{p} - \alpha_1 \le \theta \le \dfrac{2\pi}{p}) \end{cases} \tag{10}$$

To check the validity of the AM analysis of the slotless air-gap flux densities of the V-IPM machine, each air-gap flux density obtained by AM and FEM is compared in Figure 7.

The AM result shows good agreement with the FEM result, which proves the reliability of the AM result.

The Fourier series expansion of B_{m_ipm} can be calculated as

$$\begin{cases} B_{m\_ipm} = \dfrac{a_0}{2} + \displaystyle\sum_{n=1}^{\infty} B_{gn\_ipm} \cos(\frac{n\pi\theta}{l}) \\ l = \dfrac{T}{2} = \dfrac{2\pi}{p}, \end{cases} \tag{11}$$

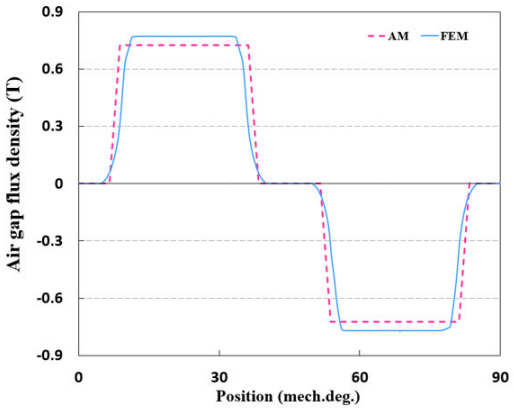

FIGURE 7. Slotless air-gap flux density waveform of the V-IPM machine.

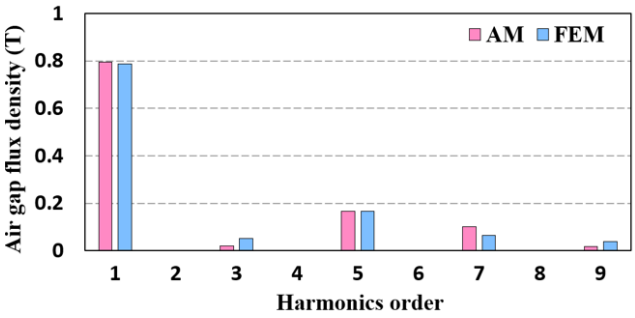

FIGURE 8. Harmonic components of the slotless air-gap flux density of the V-IPM machine.

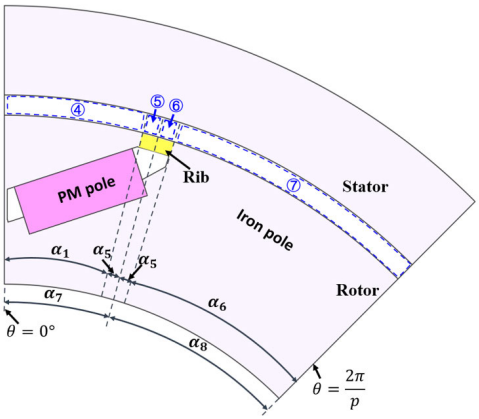

FIGURE 9. 1/8 of the V-CPM machine with the graphical description and air-gap regions.

where p is the number of poles. The value of a_0 is 0 when B_{m_ipm} is an even function, as shown in Figure 3. Hence, the equation can be expressed as

$$B_{m\_ipm} = \sum_{n=1}^{\infty} B_{gn\_ipm}\, cos\,(\frac{np\theta}{2}). \tag{12}$$

Then, the harmonic components of the slotless air-gap flux density B_{gn_ipm} can be expressed as

$$\begin{aligned} B_{gn\_ipm} &= \frac{2}{l}\int_0^{l} B_{m\_ipm}\, cos\,(\frac{np\theta}{2})d\theta \\ &= \frac{p}{\pi}\int_0^{\frac{2\pi}{p}} B_{m\_ipm}\, cos\,(\frac{np\theta}{2})d\theta \quad (\mathrm{n} = 1, 2, 3\ldots). \end{aligned} \tag{13}$$

From Eq. (10), B_{gn_ipm} also could be expressed as

$$\begin{aligned} &B_{gn\_ipm} \\ &= \frac{p}{\pi}\int_0^{\alpha_1} B_{m\_m}\, cos\,(\frac{np\theta}{2})d\theta \\ &\quad + \frac{p}{\pi}\int_{\alpha_1}^{\alpha_1+\alpha_2} \frac{B_{m\_m}}{\alpha_2}(\alpha_1+\alpha_2-\theta)\, cos\,(\frac{np\theta}{2})d\theta \\ &\quad + \frac{p}{\pi}\int_{\frac{2\pi}{p}-\alpha_1-\alpha_2}^{\frac{2\pi}{p}-\alpha_1} \frac{-B_{m\_m}}{\alpha_2}(\theta-\frac{2\pi}{p}+\alpha_1+\alpha_2)\, cos\,(\frac{np\theta}{2})d\theta \\ &\quad + \frac{p}{\pi}\int_{\frac{2\pi}{p}-\alpha_1}^{\frac{2\pi}{p}} -B_{m\_m}\, cos\,(\frac{np\theta}{2})d\theta \quad (\mathrm{n} = 1, 2, 3\ldots), \end{aligned} \tag{14}$$

where B_{m_m} is calculated in Eq. (9), the pole number p is 8.

When n is equal to 1, 2, 3, etc., the amplitude of the harmonic components of B_{gn_ipm} can be calculated, as presented in Figure 8.

B. V-CPM MACHINE

Figure 9 shows the graphical representation of the air-gap regions under one pole pair in the V-CPM machine. The flux saturation of the rotor iron is shaded with yellow. The saturated iron rib is between the PM pole and the iron pole and is divided into 2 regions. The flux line flows through the left saturation region and will return to the right saturation region, as shown in Figure 9.

The air gap facing the PM is divided into 2 regions, shown as Regions ④ and ⑤ in Figure 9. α_1 and α_5 are the corresponding angles of Regions ④ and ⑤, respectively. α_5 is half the angle of the air barrier, which is indicated as α_2 in Figure 2. The air gap-facing iron pole comprises Region ⑥ and Region ⑦. α_6 is the angle corresponding to Region ⑦. α_7 and α_8 are half of the pole-arc angle of the PM pole and iron pole, respectively. Based on the above analysis, the slotless air-gap flux density waveform in the V-IPM machine is shown in Figure 10. The directions of the air-gap flux densities in Regions ⑤ and ⑥ are opposites. Notably, the air-gap flux density waveform of V-CPM has no dead zone, as shown in Figure 10, unlike the V-IPM, as shown in Figure 3. Moreover, the amplitude of air-gap flux density for each pole is different due to the asymmetric flux distribution of the V-CPM.

The magnetic flux paths of the V-CPM machine are shown in Figure 11. Similar to the V-IPM machine, the stator steel reluctance R_s, rotor steel reluctance R_r, and air barrier reluctance R_{b1} and R_{b2} are also neglected. Unlike that of the S-CPM machine, the rotor saturation of the V-CPM machine

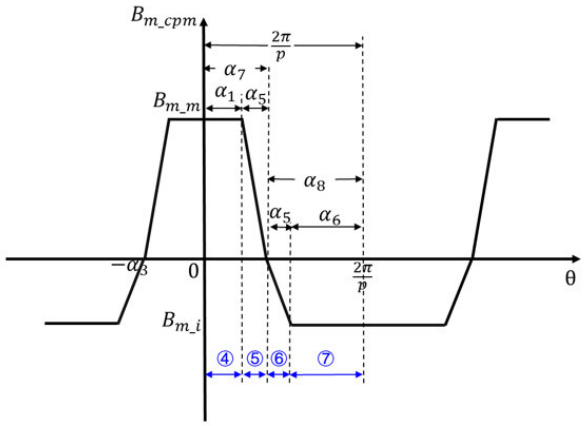

FIGURE 10. Waveform modeling of the slotless air-gap flux density of the V-CPM machine

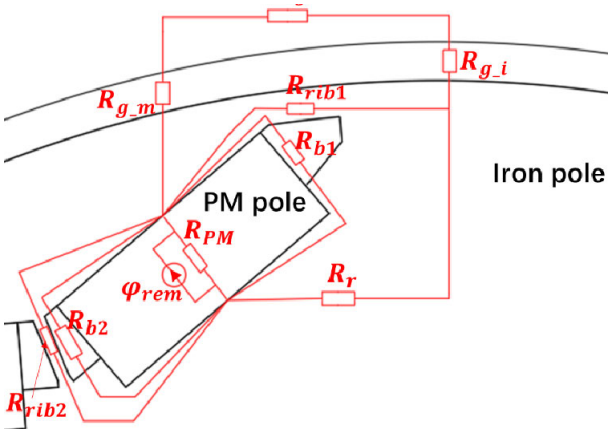

FIGURE 11. Flux paths of the V-CPM machine.

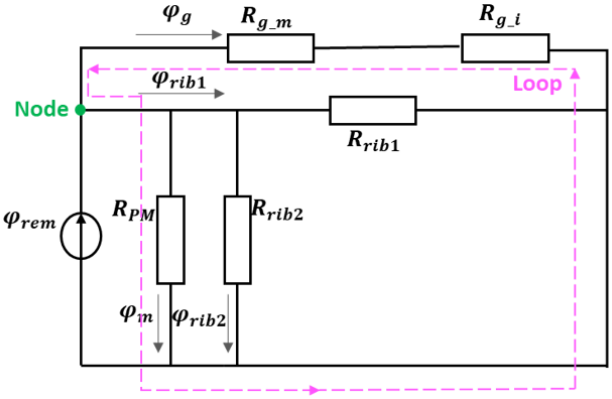

FIGURE 12. Magnetic equivalent circuit of the V-CPM machine.

is considered in the magnetic equivalent circuit. R_{rib1} and R_{rib2} are the corresponding reluctances of the two different saturation ribs. The simplified magnetic equivalent circuit of the V-CPM machine is shown in Figure 12.

In Figure 12, in contrast to the V-IPM machine, there is only one flux source φ_{rem} in the magnetic equivalent circuit under one pole pair. By applying Kirchhoff's law, the magnetic equivalent circuit equations are expressed as

$$\text{Node}: \ \varphi_{rem} = \varphi_g + \varphi_{rib1} + \varphi_{rib2} + \varphi_m, \tag{15}$$

$$\text{Loop}: \ \varphi_g^* R_{g\_m} + \varphi_g^* R_{g\_i} = \varphi_m^* R_m, \tag{16}$$

where R_{g_m} and R_{g_i} are the reluctance of the air gap in the PM pole and the iron pole, respectively. The air-gap flux density φ_g can be expressed as

$$\varphi_g = (\varphi_{rem} - \varphi_{rib1} - \varphi_{rib2})^* \left(\frac{R_m}{R_m + R_{g\_m} + R_{g\_i}}\right). \tag{17}$$

The air-gap reluctances can be expressed as

$$\begin{cases} R_{g\_m} = \dfrac{g}{\mu_0 A_{g\_m}} \\ R_{g\_m} = \dfrac{g}{\mu_0 A_{g\_i}} \end{cases}, \tag{18}$$

where A_{g_m} and A_{g_i} are the cross-sectional area of the air gap above the PM pole and the iron pole and are expressed as

$$A_{g\_m} = (R + \frac{g}{2})\alpha_7 l_{stk}, \tag{19}$$

$$A_{g\_m} = (R + \frac{g}{2})\alpha_8 l_{stk}. \tag{20}$$

The difference in the two air-gap reluctances is due to the different pole-arc angles between the PM pole and the iron pole, which are shown as α_7 and α_8 in Figure 9. The relationship between the air-gap flux density B_{m_cpm} and the air-gap flux φ_{g_1} and φ_{g_2} can be expressed as

$$\begin{cases} \varphi_{g\_1} = \displaystyle\int_0^{\theta_p} B_{m\_cpm}(\theta)(R + \frac{g}{2}) l_{stk} d\theta \\ \varphi_{g\_2} = \displaystyle\int_0^{\theta_i} B_{m\_cpm}(\theta)(R + \frac{g}{2}) l_{stk} d\theta \end{cases}, \tag{21}$$

where B_{m_cpm} is the slotless air-gap flux density of the V-CPM machine. θ_p and θ_i are half of the pole-arc angle of the PM pole and the iron pole, respectively. In V-CPM machine, $\theta_p + \theta_i = 2\pi/p$, where $\theta_p = \alpha_7$ and $\theta_i = \alpha_8$, as shown in Figure 10. φ_{g_1} and φ_{g_2} are the air-gap flux of the PM pole and the iron pole, respectively. Furthermore, according to Gauss' Law, the integration of the slotless air-gap flux density in the PM pole region is the same as the iron pole region. Hence, the air-gap flux φ_g can be expressed as

$$\varphi_g = \varphi_{g\_1} = \varphi_{g\_2}. \tag{22}$$

Thus, B_{m_m} and B_{m_i} are the maximum values of the slotless air gap in the PM and iron poles, respectively. Their values are unequal, as shown in (23) and (24).

$$B_{m\_m} = \frac{\varphi_g}{(R + \frac{g}{2})(\alpha_7 - \frac{\alpha_5}{2}) l_{stk}} = \frac{\varphi_g}{(R + \frac{g}{2})(\alpha_1 + \frac{\alpha_5}{2}) l_{stk}} \tag{23}$$

$$B_{m\_i} = -\frac{\varphi_g}{(R + \frac{g}{2})(\alpha_8 - \frac{\alpha_5}{2}) l_{stk}} = -\frac{\varphi_g}{(R + \frac{g}{2})(\frac{2\pi}{p} - \alpha_1 - \frac{3\alpha_5}{2}) l_{stk}} \tag{24}$$

The slotless air-gap flux density B_{m_cpm} could also be expressed as

$$B_{m\_m} = \begin{cases} B_{m\_m} & (0 \le \theta < \alpha_1) \\ \dfrac{B_{m\_m}}{\alpha_5}(\alpha_1 + \alpha_5 - \theta) & (\alpha_1 \le \theta < \alpha_1 + \alpha_5) \\ \dfrac{B_{m\_i}}{\alpha 5}(\theta - \alpha_1 - \alpha_5) & (\alpha_1 + \alpha_5 \le \theta < \alpha_1 + 2\alpha_5) \\ B_{m\_i} & (\dfrac{2\pi}{p} - \alpha_1 \le \theta \le \dfrac{2\pi}{p}) \end{cases} \quad (25)$$

To check the validity of the AM analysis of the slotless air-gap flux densities of the V-CPM machine, each air-gap flux density obtained by AM and FEM is compared in Figure 13.

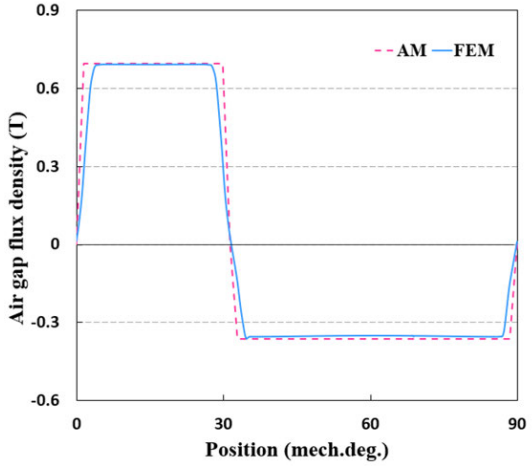

FIGURE 13. Slotless air-gap flux density of the V-CPM machine.

The AM result shows a good agreement with the FEM result. This confirms the reliability of the AM result. Because B_{m_cpm} in Figure 10 is an even function, the Fourier series expansion of the B_{m_cpm} is given as

$$B_{m\_cpm} = \sum_{n=1}^{\infty} B_{gn\_cpm}\, cos\,(\frac{np\theta}{2}). \quad (26)$$

Then, the harmonic components of the slotless air-gap flux density B_{gn_cpm} can be expressed as

$$\begin{aligned} B_{gn\_ipm} &= \frac{2}{l}\int_0^{l} B_{m\_cpm}\, cos\,(\frac{np\theta}{2})d\theta \\ &= \frac{p}{\pi}\int_0^{\frac{2\pi}{p}} B_{m\_cpm}\, cos\,(\frac{np\theta}{2})d\theta \quad (\mathrm{n} = 1, 2, 3\ldots). \end{aligned} \quad (27)$$

From Eq. (25), B_{gn_cpm} could also be expressed as

$$\begin{aligned} B_{gn\_cpm} = {} & \frac{p}{\pi}\int_0^{\alpha_1} B_{m\_m}\, cos\,(\frac{np\theta}{2})d\theta \\ & + \frac{p}{\pi}\int_{\alpha_1}^{\alpha_1+\alpha_5} \frac{B_{m\_m}}{\alpha_5}(\alpha_1 + \alpha_5 - \theta)\, cos\,(\frac{np\theta}{2})d\theta \\ & + \frac{p}{\pi}\int_{\alpha_1+\alpha_5}^{\alpha_1+2\alpha_5} \frac{B_{m\_i}}{\alpha 5}(\theta - \alpha_1 - \alpha_5)\, cos\,(\frac{np\theta}{2})d\theta \\ & + \frac{p}{\pi}\int_{\frac{2\pi}{p}-\alpha_1}^{\frac{2\pi}{p}} B_{m\_i}\, cos\,(\frac{np\theta}{2})d\theta \quad (\mathrm{n} = 1, 2, 3\ldots), \end{aligned} \quad (28)$$

where B_{m_m} and B_{m_i} are calculated in Eq. (23) and (24) and the pole number p is 8.

When n is equal to 1, 2, 3, etc., the amplitude of the harmonic components of B_{gn_cpm} can be calculated. The AM result of the proposed V-CPM machine is compared with the FEM result, as shown in Figure 14.

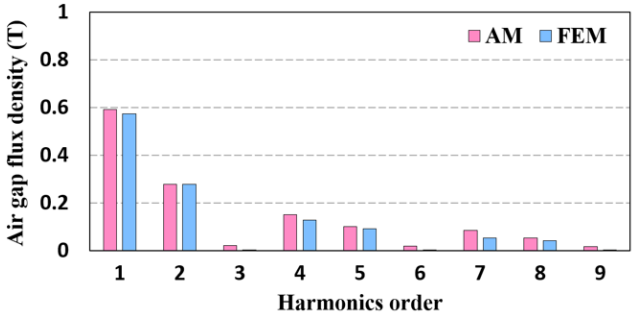

FIGURE 14. Harmonic components of the slotless air-gap flux density of the V-CPM machine.

IV. DESIGN PARAMETERS DETERMINATION AND PERFORMANCE COMPARISON

A. DETERMINATION

The target of the V-CPM design is to achieve similar average torque to that of V-IPM while decreasing the PM volume compared to V-IPM.

In general, the average torque $T_{average}$ can be expressed as

$$T_{average} = \frac{5E_0 I}{2w_r} = 5NR_a l_{stk} I w_r k_w B_{g1}, \quad (29)$$

where E_0 is the fundamental Back-EMF, I is the amplitude value of the phase current, w_r is the mechanical angular velocity of the rotor, N is number of turns per phase, R_a is the air-gap radius, k_w is the fundamental winding factor, and B_{g1} is the fundamental slotless air-gap flux density. The reluctance torque was neglected as it has only a small contribution to the output torque [8].

In Eq. (29), all parameters except B_{g1} are held the same and constant for the V-IPM and V-CPM machine designs. To achieve a similar average torque with the V-CPM machine to that of the V-IPM machine, it is designed with the same fundamental air-gap flux density. By utilizing Eq. (27) for the fundamental air-gap flux density of the V-IPM, the value can be calculated as 0.8. In Figure 16, Surface 1 corresponds to the fundamental air-gap flux density of the V-IPM machine

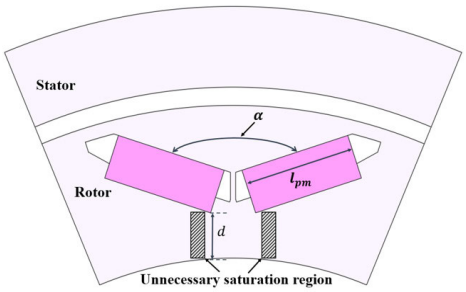

FIGURE 15. Design parameters of the V-type PM.

with a value of 0.8 ($B_{g1\_ipm} = 0.8$). Consequently, our first target can be expressed as follows:

$$B_{g1\_ipm} = B_{g1\_cpm} = 0.8. \tag{30}$$

To derive the PM volume of the designed V-CPM machine, the parameters of the PM are calculated. The PM pole-arc angle has the most crucial influence on the air-gap flux-density distribution of V-IPM machines [17], [25], [26], [27]. Furthermore, the length of the PM l_{pm} and the angle of PM α not only affect the PM pole-arc angle but also greatly affect the air-gap flux-density distribution. Thus, the PM length l_{pm} and PM angle α are set as design variables. The other parameters are kept the same as those of the V-IPM machine.

Then, the fundamental air-gap flux density of the V-CPM machine according to the variation of l_{pm} and α is calculated and can be expressed as follows:

$$B_{g1\_cpm} = f(l_{pm}, \alpha). \tag{31}$$

This is shown as Surface 2 in Figure 16, which is the fundamental air-gap flux density of the V-CPM machine according to the variation of l_{pm} and α. Line 1 is the intersection of Surfaces 1 and 2. The projection of Line 1 onto the l_{pm}- α plane is presented as a red curve in Figure 16.

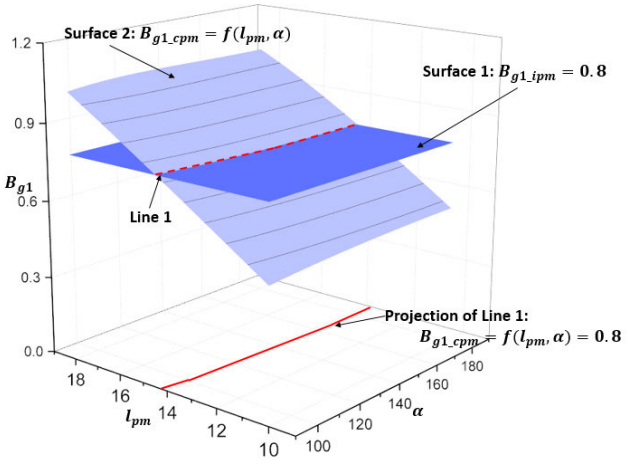

FIGURE 16. The fundamental air-gap flux density of the V-CPM machine according to the variation of l_{pm} and α.

To choose the best torque performance, namely, an average torque similar to that of V-IPM with low torque ripple, two conditions were considered from the design parameters along the projection of Line 1. These two conditions were the avoidance of unnecessary saturation and minimization of the 9th harmonic for low torque ripple [21], [28], [29].

First, the avoidance of unnecessary saturation was considered. It must be noted that if the PM is too close to the inner diameter of the rotor, unnecessary saturation will occur, as indicated in Figure 15. To avoid unnecessary saturation, the distance d from the end of the magnet to the inner diameter of the rotor is set to be greater than 2 mm. d can be expressed as

$$\begin{cases} d = (R - R_i) - [h_{pm} \sin(\dfrac{\alpha}{2}) + (l_{pm} + t_1)\, cos\, (\dfrac{\alpha}{2}) \\ + (R_b - R_b\, cos\, \alpha_1) + l_{rib1}] \\ R_b = R - l_{rib1} \end{cases} \tag{32}$$

where R_i is the inner radius of the rotor.

When A is equal to 2 mm, Eq. (32) is a function of l_{pm} and α. The relationship of l_{pm} and α in this function is shown as the saturation-prevention line in Figure 17.

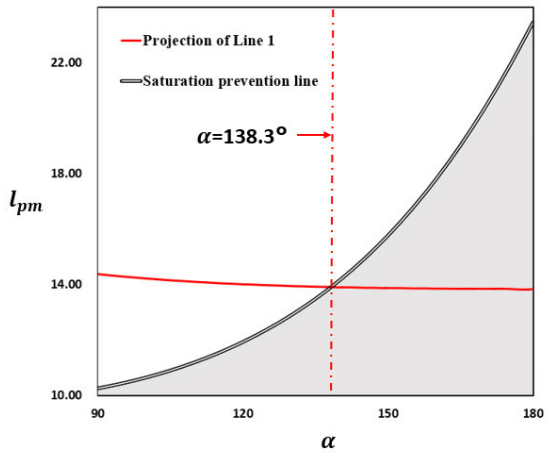

FIGURE 17. Solutions and the maximum value of l_{pm} under different α.

The maximum value of l_{pm} is applied for different α in the saturation-prevention line. The projection of Line 1 is also shown in Figure 17, where only the lower region below the saturation-prevention line meets the first condition. The saturation-prevention line and projection of Line 1 meet at $\alpha = 138.3°$. It can be concluded that only solutions with $\alpha > 138.3°$ are suitable for the V-CPM to satisfy the first condition.

Second, the 9th harmonic was minimized for low torque ripple. Because of the asymmetric air-gap flux density of consequent-pole topology, the torque ripple of the CPM machine is usually large. The analysis of the harmonic component of the air-gap flux density is utilized to reduce the torque ripple. According to [21], [28], [29], torque ripple

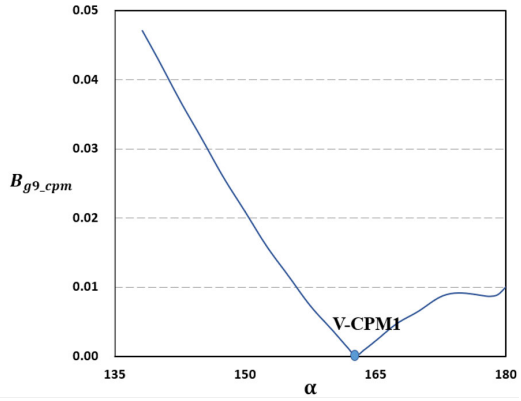

FIGURE 18. 9th harmonic of the solutions with $\alpha > 138.3°$.

occurs due to the air-gap flux density harmonic components. Among the harmonics, the 9th harmonic effects the torque ripple the most because of its correspondence to the stator MMF harmonics. Hence, the 9th harmonic was the focus of consideration. As a result, the 9th harmonic B_{g9_cpm} with α greater than 138.3° is calculated and expressed as shown in Figure 18. According to Figure 18, the smallest value of B_{g9_cpm} is found when $\alpha = 162.6°$.

Based on the selected parameter values from the above process, V-CPM1 was designed based on the α and l_{pm} values listed in Table 2. V-CPM1 was evaluated through FEM analysis in the next section.

TABLE 2. The parameters of V-CPM1.

Item	V-CPM1
l_{pm}	13.86 mm
α	162.6°

B. ELECTROMAGNETIC PERFORMANCE COMPARISON

1) OPEN-CIRCUIT AIR-GAP FLUX DENSITY

The flux-density distribution and flux lines of the V-IPM, V-CPM, and V-CPM1 machines are shown in Figure 19. The highly saturated areas around the air barriers are indicated as red circles in Figure 19, which are considered in the AM. Figure 20 shows the slotted open-circuit air-gap flux-density distribution and corresponding harmonic components of the three investigated machines. The air-gap flux density fundamental harmonic component of the V-CPM is lower than that of the V-IPM. For the V-IPM and V-CPM1 machines, the air-gap flux density fundamental harmonic components are almost equal. The air-gap flux density waveforms of the V-CPM and V-CPM1 machines are asymmetric, which results in even-order harmonics of the air-gap flux density.

2) BACK-EMF

The back-EMF waveform and its harmonic components of the V-IPM machine, the V-CPM machine and the V-CPM1

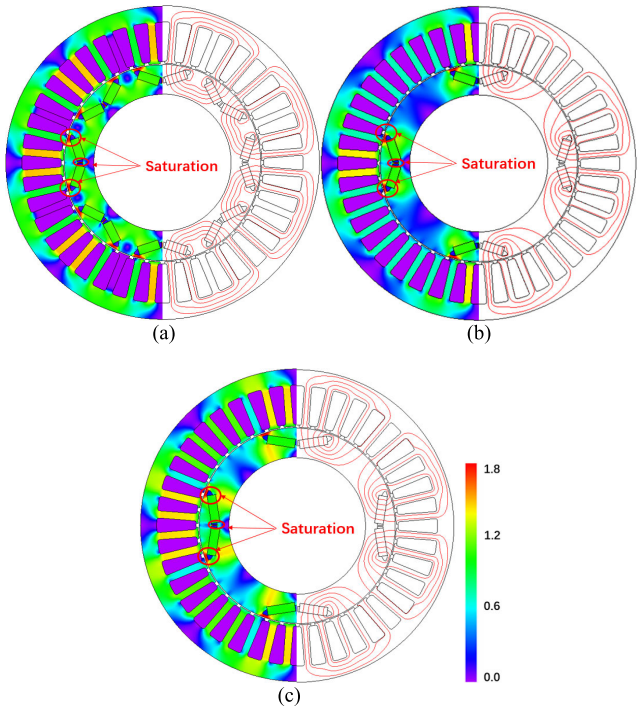

FIGURE 19. Slotless flux-density distribution (a) V-IPM (b) V-CPM (c) V-CPM1.

machine are predicted by FEM as shown in Figure 21. As shown in Figure 21 (b), the fundamental components of the back-EMF of the V-IPM, the V-CPM, and V-CPM1 machines are 82.78 V, 60.1 V, and 82.32 V, respectively. The fundamental component of the back-EMF of the V-CPM machine is much lower than that of the V-IPM machine, but the V-IPM machine and V-CPM1 machine have similar fundamental components. This is due to the similar fundamental air-gap flux density of the V-IPM and the V-CPM1 machines. Meanwhile, the difference between the back-EMF RMS values of the V-IPM and V-CPM1 machines, which are 62.5 V and 61.5 V, respectively, is less than 2%.

3) TORQUE PERFORMANCE

Figure 22 shows the cogging torque waveform of the V-IPM machine, V-CPM machine and the V-CPM1 machine, predicted by the FEM. It can be seen the cogging torque of the V-CPM1 machine is higher than that of the V-CPM and V-IPM machine. The peak-to-peak values of the cogging torque of the V-IPM machine, the V-CPM machine and the V-CPM1 machine are 0.14 Nm, 0.12 Nm, 0.25 Nm, respectively. Even though these three machines have the same stator slots and the same number of rotor poles, the cogging torques of the three machines are different because of the different no-load air-gap flux density [17].

The electromagnetic torque waveforms predicted by the FEM are shown in Figure 23. The FEM analysis results of three machines are enumerated in Table 3. The V-CPM machine has lower average torque than the V-IPM machine.

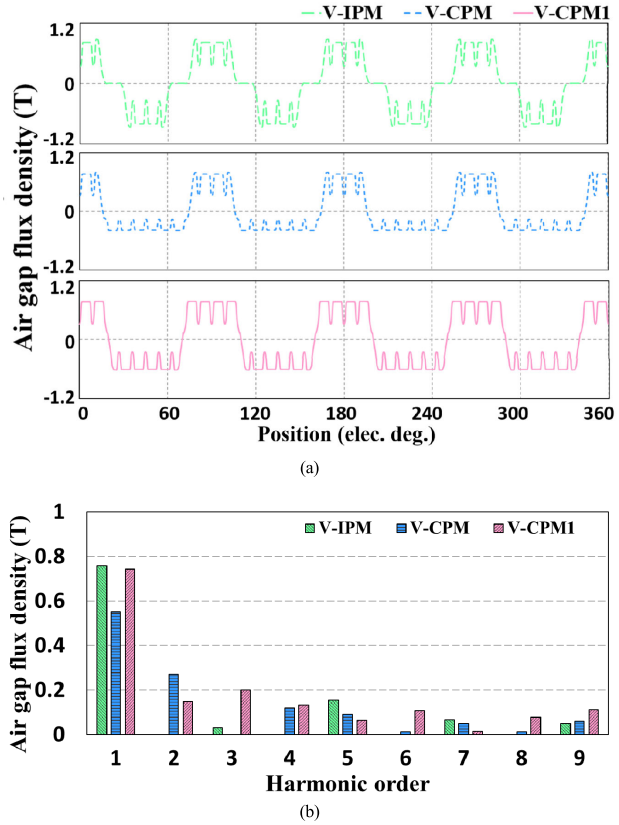

FIGURE 20. Slotted air-gap flux density (a) Waveform (b) Harmonics.

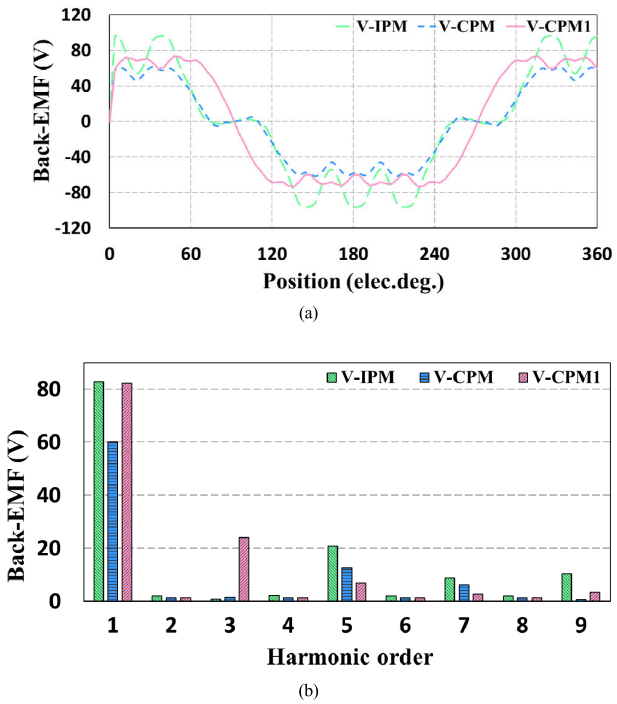

FIGURE 21. Back-EMF comparison (a) Waveform (b) Harmonics.

To obtain similar average torque to that of the V-IPM machine, V-CPM1 is designed in the previous Section. The average torque of the V-IPM, and V-CPM1 machine are 12.5 Nm and 12.2 Nm, respectively. This is because the two

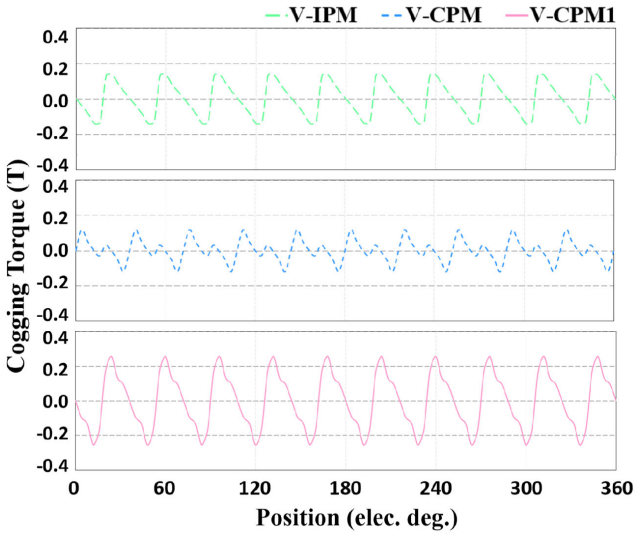

FIGURE 22. Variation of cogging torque with rotor positions.

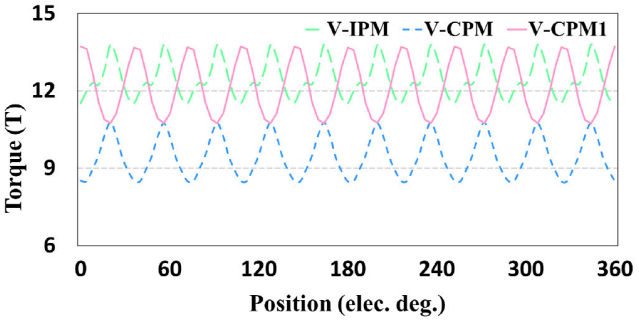

FIGURE 23. Variation of output torque with rotor positions.

TABLE 3. Characteristics of comparison.

Items	V-IPM	V-CPM	V-CPM 1
Cogging torque (Nm)	0.28	0.24	0.50
Torque (Nm)	12.5	9.36	12.2
PM volume (cm^3)	34.18 (100%)	17.09 (50%)	21.96 (64.3%)
PM utilization ratio (η)	0.366 (100%)	0.547 (149.6%)	0.555 (151.3%)
Efficiency	90.7%	88.2%	90.7%
Torque ripple	18.0%	24.3%	24.2%

machines have almost the same fundamental air-gap flux density. Meanwhile, compared with the V-IPM machine, the V-CPM1 achieves similar average torque with less PM volume. To highlight the usage of PM clearly, the PM utilization ratio is utilized. PM utilization ratio is defined as follows:

$$PM\text{utilization ratio } \eta = \frac{Torque}{PM \text{ volume}}. \tag{33}$$

Although the V-CPM machine has lower average torque than the V-IPM machine, the PM utilization is increased.

As listed in Table 3, the PM utilization ratio of the V-CPM machine and the V-CPM1 machine are greatly increased by 49.6% and 51.3%, respectively, compared to that of the V-IPM machine. This indicates that the CPM topology could improve PM utilization. The V-IPM machine and the V-CPM1 machine have similar efficiencies, owing to their similar output power and iron loss. This indicates that when the V-CPM1 is used to replace the V-IPM machine, the efficiency consideration could be negligible. Therefore, it can be said that the V-CPM1 machine can achieve the target torque performance with reduced PM cost compared with the V-IPM machine. Even the torque ripple of the V-CPM1 machine is somewhat larger than that of the V-IPM, but V-CPM1 can replace the V-IPM machine in some applications when the torque ripple is not strictly specified.

V. CONCLUSION

This paper proposed an AM for the design of V-CPM machine to reduce the PM volume and retain a similar average torque compared to that of the V-IPM machine. An AM for the slotless model of V-IPM and V-CPM machines was proposed with different air-gap regions. The slotless air-gap flux-density distribution and amplitude of the harmonic components of the V-IPM and V-CPM machines were calculated with a constructed magnetic equivalent circuit. In particular, the constructed magnetic equivalent circuit for V-CPM considered the unique magnetic saturation in the rotor part of the V-CPM. The design target of the V-CPM was to achieve similar average torque to that of the V-IPM machine while reducing the PM volume. Hence, the fundamental air-gap flux density of the V-CPM was designed to be equal to that of the V-IPM machine. Then, to achieve the best torque performance of the V-CPM machine, two conditions were considered. V-CPM1 was designed by considering these two conditions; hence, unnecessary saturation and torque ripple were minimized while maintaining the average torque. The performance of the V-IPM, V-CPM, and V-CPM1 machines were analyzed and compared with the aid of FEM. As a result, the V-CPM1 machine achieved similar average torque with a 36.7 % reduction of PM volume compared to that of the V-IPM machine. The PM utilization ratio has increased by 51.3 % accordingly. However, due to the cogging torque increase, the torque ripple of V-CPM1 has increased 6.2 % more compared to the V-IPM. The results indicated that the V-CPM1 machine had good agreement with the average torque of the V-IPM machine, even with reduced PM volume. Moreover, the duration of the AM was much less than that of the FEM. Hence, it was demonstrated that the proposed AM is an attractive method to design V-CPM machines in various applications.

REFERENCES

[1] G. Xu, G. Liu, W. Zhao, Q. Chen, and X. Du, "Principle of torque-angle approaching in a hybrid rotor permanent-magnet motor," *IEEE Trans. Ind. Electron.*, vol. 66, no. 4, pp. 2580–2591, Apr. 2019.
[2] Z. Yang, F. Shang, I. P. Brown, and M. Krishnamurthy, "Comparative study of interior permanent magnet, induction, and switched reluctance motor drives for EV and HEV applications," *IEEE Trans. Transport. Electrific.*, vol. 1, no. 3, pp. 245–254, Oct. 2015.
[3] G. Pellegrino, A. Vagati, P. Guglielmi, and B. Boazzo, "Performance comparison between surface-mounted and interior PM motor drives for electric vehicle application," *IEEE Trans. Ind. Electron.*, vol. 59, no. 2, pp. 803–811, Feb. 2012.
[4] J. Li, K. Wang, and C. Liu, "Torque improvement and cost reduction of permanent magnet machines with a dovetailed consequent-pole rotor," *IEEE Trans. Energy Convers.*, vol. 33, no. 4, pp. 1628–1640, Dec. 2018.
[5] J. Li, K. Wang, and F. Li, "Reduction of torque ripple in consequent-pole permanent magnet machines using staggered rotor," *IEEE Trans. Energy Convers.*, vol. 34, no. 2, pp. 643–651, Jun. 2019.
[6] Z. Li, Y. Li, and X. Li, "Flux control of a CPPM machine for both a wide speed range and high efficiency," *IEEE Trans. Power Electron.*, vol. 29, no. 9, pp. 4866–4876, Sep. 2014.
[7] J. Li and K. Wang, "A novel spoke-type PM machine employing asymmetric modular consequent-pole rotor," *IEEE/ASME Trans. Mechatronics*, vol. 24, no. 5, pp. 2182–2192, Oct. 2019.
[8] J. Li, K. Wang, and H. Zhang, "Flux-focusing permanent magnet machines with modular consequent-pole rotor," *IEEE Trans. Ind. Electron.*, vol. 67, no. 5, pp. 3374–3385, May 2020.
[9] W. Chai, J.-W. Kwon, and B.-I. Kwon, "Analytical design of a hybrid-excited wound field synchronous machine for the improvement of torque characteristics," *IEEE Access*, vol. 8, pp. 87414–87421, 2020.
[10] H.-K. Yeo, D.-K. Lim, and H.-K. Jung, "Magnetic equivalent circuit model considering the overhang structure of an interior permanent-magnet machine," *IEEE Trans. Magn.*, vol. 55, no. 6, pp. 1–4, Jun. 2019.
[11] G. Liu, L. Liu, Q. Chen, and W. Zhao, "Torque calculation of five-phase interior permanent magnet machine using improved analytical method," *IEEE Trans. Energy Convers.*, vol. 34, no. 2, pp. 1023–1032, Jun. 2019.
[12] A. Rahideh and T. Korakianitis, "Analytical magnetic field calculation of slotted brushless permanent-magnet machines with surface inset magnets," *IEEE Trans. Magn.*, vol. 48, no. 10, pp. 2633–2649, Oct. 2012.
[13] J. Amemiya, A. Chiba, D. G. Dorrell, and T. Fukao, "Basic characteristics of a consequent-pole-type bearingless motor," *IEEE Trans. Magn.*, vol. 41, no. 1, pp. 82–89, Jan. 2005.
[14] J. Asama, M. Amada, M. Takemoto, A. Chiba, T. Fukao, and A. Rahman, "Voltage characteristics of a consequent-pole bearingless PM motor with concentrated windings," *IEEE Trans. Magn.*, vol. 45, no. 6, pp. 2823–2826, Jun. 2009.
[15] S. Teymoori, A. Rahideh, H. Moayed-Jahromi, and M. Mardaneh, "2-D analytical magnetic field prediction for consequent-pole permanent magnet synchronous machines," *IEEE Trans. Magn.*, vol. 52, no. 6, pp. 1–14, Jun. 2016.
[16] A. Ghaffari, A. Rahideh, H. Moayed-Jahromi, A. Vahaj, A. Mahmoudi, and W. L. Soong, "2-D analytical model for outer-rotor consequent-pole brushless PM machines," *IEEE Trans. Energy Convers.*, vol. 34, no. 4, pp. 2226–2234, Dec. 2019.
[17] J. Li and K. Wang, "Analytical determination of optimal PM-arc ratio of consequent-pole permanent magnet machines," *IEEE/ASME Trans. Mechatronics*, vol. 23, no. 5, pp. 2168–2177, Oct. 2018.
[18] J. Li, K. Wang, and F. Li, "Analytical prediction of optimal split ratio of consequent-pole permanent magnet machines," *IET Electric Power Appl.*, vol. 12, no. 3, pp. 365–372, Mar. 2018.
[19] S. Taghipour Boroujeni, S. P. Emami, N. Takorabet, and A. Mahmoudi, "Analytical investigation of the armature current influence on the torque and radial force in eccentric consequent-pole PM machines," *IET Electr. Power Appl.*, vol. 15, no. 4, pp. 441–452, Apr. 2021.
[20] J. Kolehmainen, "Optimal dovetail permanent magnet rotor solutions for various pole numbers," *IEEE Trans. Ind. Electron.*, vol. 57, no. 1, pp. 70–77, Jan. 2010.
[21] Q. Chen, G. Xu, G. Liu, W. Zhao, L. Liu, and Z. Lin, "Torque ripple reduction in five-phase IPM motors by lowering interactional MMF," *IEEE Trans. Ind. Electron.*, vol. 65, no. 11, pp. 8520–8531, Nov. 2018.
[22] M. Farshadnia, M. A. M. Cheema, R. Dutta, and J. E. Fletcher, "Analytical modeling of armature reaction air-gap flux density considering the non-homogeneously saturated rotor in a fractional-slot concentrated-wound IPM machine," *IEEE Trans. Magn.*, vol. 53, no. 2, pp. 1–12, Feb. 2017.
[23] K. Ahsanullah, R. Dutta, and M. F. Rahman, "Investigation of flat and V-shaped magnets in interior permanent magnet machine for direct drive wind turbine application," in *Proc. IEEE ECCE Asia Downunder*, Jun. 2013, pp. 208–213.

[24] A. B. Proca, A. Keyhani, A. EL-Antably, W. Lu, and M. Dai, "Analytical model for permanent magnet motors with surface mounted magnets," *IEEE Trans. Energy Convers.*, vol. 18, no. 3, pp. 386–391, Sep. 2003.
[25] S.-U. Chung, J.-W. Kim, Y.-D. Chun, B.-C. Woo, and D.-K. Hong, "Fractional slot concentrated winding PMSM with consequent pole rotor for a low-speed direct drive: Reduction of rare Earth permanent magnet," *IEEE Trans. Energy Convers.*, vol. 30, no. 1, pp. 103–109, Mar. 2015.
[26] D. Li, R. Qu, J. Li, and W. Xu, "Consequent-pole toroidal-winding outer-rotor Vernier permanent-magnet machines," *IEEE Trans. Ind. Appl.*, vol. 51, no. 6, pp. 4470–4481, Nov. 2015.
[27] Z. Z. Wu and Z. Q. Zhu, "Partitioned stator flux reversal machine with consequent-pole PM stator," *IEEE Trans. Energy Convers.*, vol. 30, no. 4, pp. 1472–1482, Dec. 2015.
[28] S.-H. Han, T. M. Jahns, and W. L. Soong, "Torque ripple reduction in interior permanent magnet synchronous machines using the principle of mutual harmonics exclusion," in *Proc. IEEE Ind. Appl. Annu. Meeting*, Sep. 2007, pp. 558–565.
[29] S.-H. Han, T. M. Jahns, W. L. Soong, M. K. Guven, and M. S. Illindala, "Torque ripple reduction in interior permanent magnet synchronous machines using stators with odd number of slots per pole pair," *IEEE Trans. Energy Convers.*, vol. 25, no. 1, pp. 118–127, Mar. 2010.

JUNG-WOO KWON was born in 1992. He received the B.S. degrees in bio-nano engineering and electrical engineering, and the M.S. and Ph.D. degrees from Hanyang University, Ansan, South Korea, in 2015 and 2019, respectively. He is currently working as a Postdoctoral Researcher with the Department of Electrical and Electronic Engineering, Hanyang University. His research interest includes electric machines, especially on motors.

MINGJIE LI was born in Hubei, China, in 1995. He received the B.S. degree in automation from the Chongqing University of Science and Technology, Chongqing, China, in 2016. He is currently pursuing the M.S. degree in electrical engineering with the Department of Electrical and Electronic Engineering, Hanyang University, Ansan, South Korea. His research interest includes design, analysis, and modeling of electric machines.

BYUNG-IL KWON (Senior Member, IEEE) was born in 1956. He received the B.S. and M.S. degrees in electrical engineering from Hanyang University, Ansan, South Korea, in 1981 and 1983, respectively, and the Ph.D. degree in electrical engineering and machine analysis from The University of Tokyo, Tokyo, Japan, in 1989.

From 1989 to 2000, he was a Visiting Researcher with the Faculty of Science and Engineering Laboratory, University of Waseda, Tokyo. In 1990, he was a Researcher with the Toshiba System Laboratory, Yokohama, Japan. In 1991, he was a Senior Researcher with the Institute of Machinery and Materials Magnetic Train Business, Daejeon, South Korea. From 2001 to 2008, he was a Visiting Professor with the University of Wisconsin–Madison, Madison, WI, USA. He is currently a Professor with Hanyang University. His research interest includes design and control of electric machines.